Wavelike dynamics for high harmonic generation in solids

Hubin Cui,[1] Liang Li [1,*] Yuntian Zhang [1] Sen Qiao,[1] Di Wu,[1] Pengfei Lan,[1,†] and Peixiang Lu [1,2,3]

[1]*School of Physics and Wuhan National Laboratory for Optoelectronics, Huazhong University of Science and Technology, Wuhan 430074, China*
[2]*Hubei Key Laboratory of Optical Information and Pattern Recognition, Wuhan Institute of Technology, Wuhan 430205, China*
[3]*CAS Center for Excellence in Ultra-intense Laser Science, Shanghai 201800, China*

We investigate the wavelike dynamics for high harmonic generation (HHG) in solids. Our results indicate that the wavelike behavior of electrons plays a crucial role in HHG process of solids. In solids, the group velocity dispersion, i.e., the second derivative of energy band, can lead to substantial spatial spread for the evolution of the electron wave packet. This kind of wavelike effect is embedded in the interference of electron-hole wavelets, and allows electrons and holes to be separated spatially when emitting HHG. Incorporating the wavelike effect, we show how one can understand the time-frequency properties of HHG from the perspective of wavelike picture. Furthermore, taking the gapped graphene as a prototype, we also demonstrate that the wavelike picture can well describe the two-dimensional electron dynamics and the emission intensity of HHG. Our analysis provides a comprehensive understanding of the HHG emission properties in solids, and shows how to comprehend the underlying electron dynamics from the perspective of wavelike picture.

I. INTRODUCTION

High harmonic generation (HHG), resulting from the nonperturbative interaction between an intense laser and gaseous targets, has established the foundation for attosecond science [1,2]. Recently, HHG has also been observed in condensed matters [3–8]. Since its first observation, HHG in solids has attracted significant attention due to its broad applications in generating ultrashort XUV radiation [6,9] and probing the structures [6,10–17] or ultrafast electronic dynamics of solids [6,18,19].

For atomic gases, the HHG can be interpreted using the recollision picture [2,20]. Driven by a laser, the liberated electrons are largely free from the influence of the ion core, and thus a particlelike description on electrons can capture the essential feature of HHG emission. Recently, the recollision picture was also extended to solids [21–23]. However, unlike the atomic case, electrons in solids are delocalized, and the impact of the lattice's periodic potential on electronic motion is significant. This suggests that electrons can be scattered by the lattice or recombine at different sites, complicating the microscopic electronic dynamics [24–27]. Recently, several studies have demonstrated that the emission time and energy predicted by particlelike recollision picture shows significant deviation from the simulations of semiconductor Bloch equations (SBEs) [28–30]. In Ref. [28], a four-step model has been proposed, and an additional preacceleration step prior to ionization is demonstrated to play an important role in solid HHG. Considering the spatially delocalized nature of the

real-space electron wave packet, it has also been found that the imperfect recollision for electrons and holes is general for systems with large Berry curvatures [29], or in any system driven by elliptically polarized light [28,31,32]. Furthermore, in light of the wave-particle duality, a wavelike picture has been proposed to describe HHG in solids [30,33]. This model characterizes HHG as the interference of a collection of electron-hole wavelets, drawing parallels with the Huygens-Fresnel principle. This approach incorporates wave properties into the interference process, thereby can well describe the emission characteristics of solid HHG.

In this study, we investigate the wavelike dynamics of electrons to delve deeper into the fundamental mechanism of solid HHG. Previously, the recollision model mainly concerns the particlelike motion of electron-hole pairs from the trajectories determined by the velocity difference between the conduction and valence bands. Whereas, we demonstrate that it is not sufficient to fully describe the electronic dynamics due to the neglect of wavelike behavior of electrons. Our results indicate that the wavelike effect caused by the group velocity dispersion (GVD) can not be ignored in solids, which can influence the dynamics of electron wave packet and cause significant spatial spread. The wavelike effect is embedded in the interference process of HHG, and permits the electrons and holes to be separated spatially when emitting HHG. Taking into account the wavelike behavior of electrons and holes, we show how to understand the time-frequency properties of HHG emission from the perspective of wavelike picture. In addition, in noncentrosymmetrical gapped graphene, we took into account the Berry phase and dipole phase. We further show that the wavelike picture is also able to describe the two-dimensional (2D) electron-hole dynamics, as well the emission intensity. In essence, we provide an in-depth

*liangl@hust.edu.cn
†pengfeilan@hust.edu.cn

195206-1

understanding of emission properties and reveal the associated electronic dynamics for solid HHG.

II. WAVELIKE DYNAMICS BASED ON INTERFERENCE PRINCIPLE

A. Theoretical model

We consider a two-band model of ZnO [21] with a fully filled valence band (VB) and an empty conduction band (CB) initially. Within the parameters used in this work, the contribution of the interband emission is dominant for the harmonics in the plateau region. Therefore, we only consider the interband emission, which is usually formulated as a multiple integrals using the Keldysh approximation [21,28,30]. Following the saddle-point integral for the interband current, the recollision picture is established based on three saddle-point equations [21], which represent the ionization, acceleration, and recollision processes of electron-hole pairs, respectively. We call it the classical saddle-point method (CSPM) in this work. Differently, in Ref. [30], the interband current can also be tackled with the Gaussian integral. In this context, the HHG emission observed at time t_r can be interpreted as the interference of all wavelets ionized at different initial momenta k_l and times t':

$$Y(\Omega, t_r) \propto \left| \sum_{k_l, t' \in [0, t_r]} f(k_l, t') P(k_l, t_r, t') e^{-iS(k_l, t_r, t')} \right|^2, \quad (1)$$

where $Y(\Omega, t_r)$ is the harmonic yield, $f(k_l, t')$ and $P(k_l, t_r, t')$ describe the ionization and emission amplitudes, respectively, and $S(k_l, t_r, t')$ is the phase of wavelet. Unlike the particlelike recollision, the HHG emission is built on the constructive interference of wavelets in both time domain (t') and momentum space (k_l).

For the electrons ionized from an individual momentum k_l, the constructive interference for time domain (t') lies on the condition of slow-varying phase, i.e., the partial derivative with respect to t':

$$|\partial_{t'} S| = |\Delta\varepsilon_{cv}(k_l) - x(k_l, t_r, t') F(t')| \quad (2)$$

reaches a minimum. Here, $\Delta\varepsilon_{cv}$ is the band gap between the conduction band and valence band, $x(k_l, t_r, t') = \int_{t'}^{t_r} \partial_k \Delta\varepsilon_{cv}(k_l, \tau, t') d\tau$ is the classical electron-hole displacement, $F(t')$ is the electric field amplitude. Following this condition, we can determine the most probable ionization time and the corresponding central emission energy $\Omega_c = \Delta\varepsilon_{cv}(k_l, t_r, t_i)$. Then, the HHG can be approximately considered as the superposition of all time-domain constructive interference contributed by different ionization momenta k_l (for a detailed elaboration, one can refer to Appendix A). In general, the central emission frequencies for each ionization momentum distribute in a narrow range of frequency domain. Therefore, we can adopt the central frequency of the distribution to represent the overall HHG emission. We call this method the wavelet stationary-phase method (WSPM).

In Fig. 1, we employ two different electric fields to illustrate the effectiveness of WSPM. Atomic units are used throughout this work unless indicated otherwise. The central frequencies for these two fields are the same $\omega_0 = 0.0152$ a.u.,
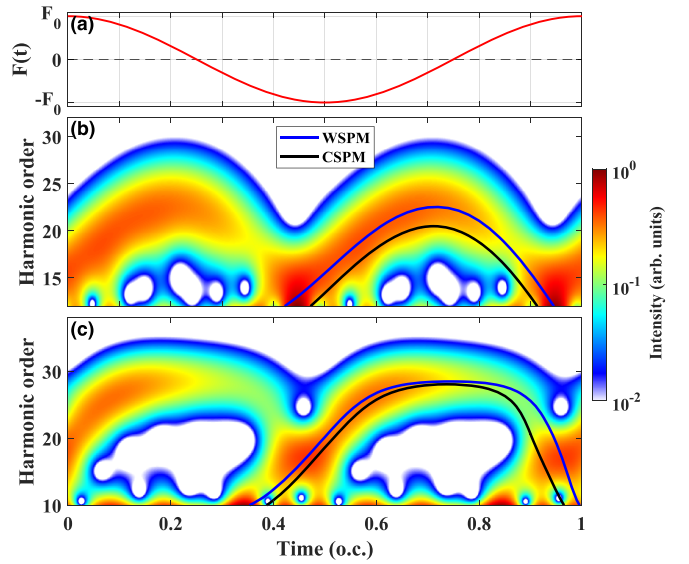

FIG. 1. (a) The temporal shape of the electric field amplitude $F(t)$. The time-frequency properties simulated with SBEs for two electric fields with same frequency $\omega_0 = 0.0152$ a.u., but different field strength $F_0 = 0.003$ a.u., (b) and $F_0 = 0.0048$ a.u. (c). The blue lines represent the central emission frequency predicted by WSPM. The black lines represent the central emission frequency predicted by CSPM.

and the amplitudes are $F_0 = 0.003$ a.u. [Fig. 1(b)] and $F_0 = 0.0048$ a.u. [Fig. 1(c)] respectively. The corresponding time frequency properties are simulated with SBEs, and the results from one cycle are shown in Figs. 1(b) and 1(c). For clarity, the temporal shape of the field amplitude $F(t)$ within one cycle is also displayed in Fig. 1(a). For comparison, the central emission energy as a function of emission time (we call it the emission channel) predicted by WSPM and CSPM is presented with blue and black lines, respectively. It can be seen that the predictions of WSPM match well with the simulations of SBEs for both low and high field strength. From the analysis in WSPM, we can know the interference of electron-hole wavelets plays a crucial role in HHG process. On the contrary, the predictions of CSPM deviate from the simulation of SBEs in both of the emission time (about 500 attoseconds) and energy (about $2 \sim 4\omega_0$) for low field strength, while close to the simulation of SBEs for high field strength. These results imply that the deviation of CSPM arises from the neglected wavelike effect embedded in the interference of wavelets. Such wavelike effect is more significant for low field strength.

B. Role of GVD in HHG process

According to our previous discussion, the interference of wavelets plays a crucial role in the HHG process. In this section, we aim to uncover the wavelike dynamics underlying the time-domain interference process. For this purpose, we focus on the contribution of a single ionization momentum $k_l = 0$ [seen in Fig. 2(a)], which can encapsulate the primary feature of total HHG emission. Here, we adopt the same electric field used in Fig. 1(a). As discussed previously, the constructive interference in time domain occurs at the minimum of Eq. (2).
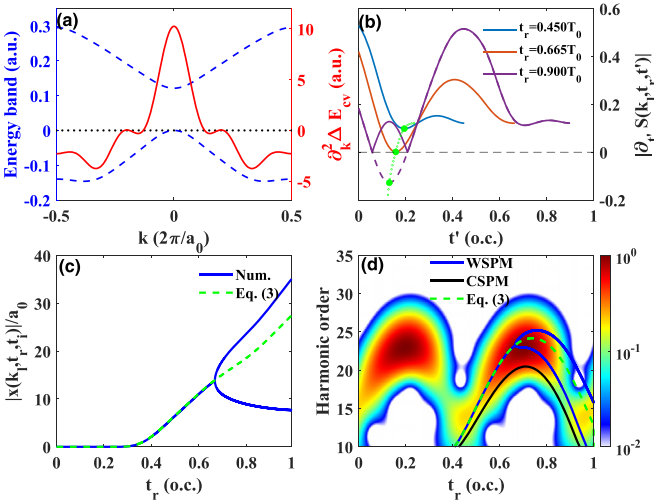
FIG. 2. (a) The ZnO energy band and the second derivative of band gap. (b) The value of $|\partial_{t'}S|$ for three different emission times: 0.45 T_0, 0.665 T_0, 0.900 T_0. The amplitude and frequency of electric field used here are $F_0 = 0.003$ a.u. and $\omega_0 = 0.0152$ a.u., respectively. (c) The numerical (blue lines) and analytic (green line) electron-hole distance predicted by the WSPM. (d) The time-frequency profile contributed by the ionization momentum $k_l = 0$, and the emission channels predicted by WSPM (blue line), CSPM (black line), and Eq. (3) (green line).

Figure 2(b) displays the value of Eq. (2) with respect to t' for three different emission times $t_r = 0.450\,T_0$ (blue line), $t_r = 0.665\,T_0$ (orange line) and $t_r = 0.900\,T_0$ (purple line) with $T_0 = \frac{2\pi}{\omega_0}$ the laser period, and the minima are marked with dots. We denote the time $t_r = 0.665\,T_0$ as t_s. It is worth to note that there is one minimum for $t_r \leqslant t_s$. For $t_r > t_s$, there are two minima with zero value, we adopt the medium temporal position to represent their average level. Obviously, the minimum satisfies the condition $\partial_{t'}^2 S = 0$. By solving this equation, we can derive the expression for electron-hole distance:

$$x(k_l, t_r, t_i)$$
$$= \frac{F(t_i)\partial_k \Delta\varepsilon_{cv}(k_l) - F^2(t_i)\int_{t_i}^{t_r} \partial_k^2 \Delta\varepsilon_{cv}(k_l, \tau, t_i)d\tau}{\partial F/\partial t'|_{t_i}}. \quad (3)$$

Here, the first term on the right side is minimal near the minimum band gap (exactly zero at $k_l = 0$), hence, our focus is on the second term. The second term involves the integral of the second derivative of energy dispersion, i.e., the GVD, within the accelerating interval $[t', t_r]$. Figure 2(a) shows the second derivative of the band gap with a solid red line. Figure 2(c) illustrates that the nonzero electron-hole distance determined numerically (blue line) and analytically by solving Eq. (3) (dashed green line), respectively. One can see that they are consistent for $t_r \leqslant t_s$. It is demonstrated that the existence of GVD can allow a nonzero separation for electron and hole when emitting HHG.

To elucidate the role of GVD in electron motion, we simulate the evolution of an electronic wave packet in Appendix B. We find that the GVD significantly influences wave-packet dynamics, resulting in considerable spatial spread. From

Eq. (3), it is inferred that the spatial spread effect contributes to the delocalized emission in solids, permitting the electron and hole to be separated spatially when emitting HHG. In contrast, the CSPM discards the wavelike effect, failing to fully capture the spatial property of electron motion. This limitation hinders the ability of CSPM to describe HHG process in solids. To illustrate this point, we compare the results of CSPM and WSPM with the time-frequency spectra simulated with SBEs in Fig. 2(d). Here, the time-frequency spectra are obtained from the Gabor transformation of interband current contributed by a single ionization channel $k_l = 0$. We note that the interband current for a single channel k_l is simulated with SBEs by multiplying a Gaussian window $\exp[-\frac{(k-k_l)^2}{g_k^2}]$ (with $g_k = 0.01\frac{\pi}{a_0}$, and a_0 the lattice constant) to the transition term, i.e., $F(t)X_{cv}(k)$, with X_{cv} the transition dipole. Apparently, the emission structure predicted by CSPM (black line) deviates from the SBEs simulations in emission time and energy. In contrast, the predictions of WSPM (blue lines) closely align with the simulations of SBEs. Meanwhile, the analytic prediction of Eq. (3) (dashed green line) is also consistent with the numerical result (blue line) up until $t_r = t_s$. Definitely, the GVD plays a crucial role in wavelike dynamics of electrons, and influences the emission properties of solid-state HHG.

In the discussion above, we have considered the phase up to the second-order expansion, which is enough to describe the primary time-frequency feature, i.e., the relation between the central emission energy and the emission time. For more detailed structure, it is necessary to expand the phase to the higher orders at the ionization time t_i: $S(t') = S(t_i) + S'(t_i)(t' - t_i) + S'''(t_i)(t' - t_i)^3 + S''''(t_i)(t' - t_i)^4 + \cdots$. The higher derivatives $S'''(t_i)$ and $S''''(t_i)$ include the terms of group delay dispersion (GDD), which is defined on the third-order derivative of energy band, i.e., $\partial_k^3 \Delta\varepsilon_{cv}$. Apparently, the GDD will affect the rate of phase change in the vicinity of t_i, and determine the emission distribution around the central emission frequency (a detailed discussion can be found in Appendix B).

In addition, our model also forecasts a unique phenomenon: the emission channel bifurcates into two parts when $t_r > t_s$, though one of them with higher emission energy does not seem clear. This characteristic, akin to multiple interference fringes in optics, is a typical wavelike feature not existing in the CSPM. We will demonstrate and elucidate this phenomenon in Secs. III A and III B. According to Eq. (2), the electron-hole distances for these two channels can be expressed by $x(k_l, t_r, t_i) = \Delta\varepsilon_{cv}(k_l)/F(t_i)$. Apparently, when $F(t_i) \neq 0$, the electron-hole distance will approach to zero for a tiny band gap. That is to say, the predictions of WSPM and CSPM will become closer for the cases of smaller band gaps. In addition, it is worth to note that these two split channels diverge almost symmetrically from that determined by Eq. (3) [represented by the dashed green line in Fig. 2(d)]. Therefore, Eq. (3) can still represent the average level of the two channels, and describe the primary emission properties.

C. Dependence of CSPM's deviation on the laser parameters

In previous discussions, we notice that the deviation of CSPM is different for high and low field strength. Therefore, we will further discuss the deviation of CSPM across different laser parameters, and unravel its dependence on laser parame-
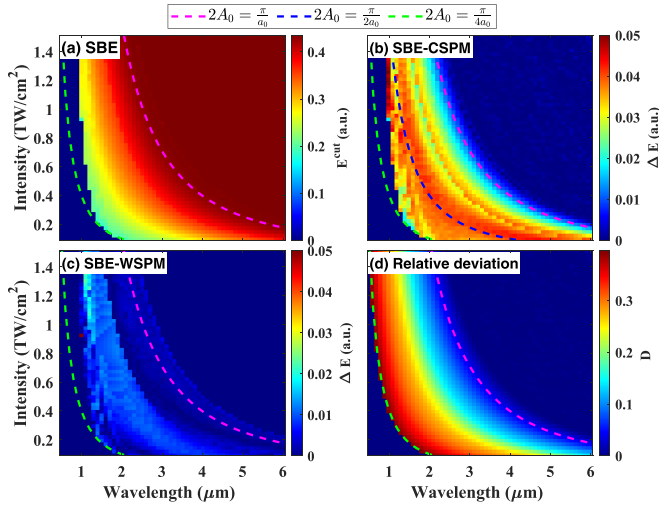
FIG. 3. (a) The cutoff energy extracted from the time-frequency profiles simulated by SBEs for different electric field parameters. (b) The absolute deviation of the cutoff energy between the CSPM and SBEs. (c) Same as (b), but between the WSPM and SBEs. (d) The relative deviation between WSPM and CSPM.

ters. We use the cutoff energy as a metric to evaluate the deviation. Figure 3(a) displays the cutoff energy obtained from the SBEs simulations across different laser parameters. We note that the cutoff energy is extracted from the time-frequency profiles for accuracy. Here, we only consider the parameter region between the dashed green ($2A_0 = \pi/4a_0$, $A_0 = \frac{F_0}{\omega_0}$ is the peak amplitude of laser vector potential) and magenta ($2A_0 = \pi/a_0$) lines. This is because the intraband emission dominates for the region below the dashed green line, while the cutoff energy reaches the maximum of band gap and becomes saturated for the region above the dashed magenta line. In the region we considered, one can see that the cutoff energy increases synchronously with the laser vector potential.

The deviations of CSPM and WSPM from the SBE simulations are displayed in Figs. 3(b) and 3(c), respectively. One can see that the deviation of CSPM is significant, and shows an obvious dependence on the laser vector potential A_0,

reaching a maximum about 0.05 a.u. (corresponding to about 2 and 5 harmonic orders for wavelength 1.5 and 5 μm) near $2A_0 = \pi/2a_0$ (dashed blue line). In contrast, there is only a minor deviation below 0.01 a.u. for WSPM. This suggests that the WSPM is robust across different parameters. Additionally, considering the nonlinearity of the energy band, we further introduce the relative deviation, which is defined as below:

$$D = \frac{E_{\mathrm{WSPM}}^{\mathrm{cut}} - E_{\mathrm{CSPM}}^{\mathrm{cut}}}{E_{\mathrm{WSPM}}^{\mathrm{cut}} - E_g^{\mathrm{min}}}, \tag{4}$$

where E_g^{min} represents the minimum band gap. The corresponding result is depicted in Fig. 3(d). One can see that the relative deviation decreases monotonically with laser vector potential in the region between dashed green and magenta lines. To understand this parameter dependence intuitively, we display the results along a vertical line in the parameter space with a fixed laser wavelength but varying intensity from 0.125 TW/cm² to 0.8 TW/cm² in Figs. 4(a)–4(j). Apparently, the relative deviation decreases noticeably with the optical intensity.

As we have previously demonstrated, the deviation of CSPM mainly arises from the overlooked wavelike effects caused by the GVD. This inspires us to understand the parameter dependence from the perspective of wavelike dynamics. In the wavelike picture, the emission condition is determined by Eq. (3). For brevity, we perform a variable substitution $\phi = \omega_0\tau$:

$$\int_{\phi_i^w}^{\phi_r} \partial_k \Delta\varepsilon_{cv}(k_l, \phi, \phi_i^w) d\phi$$

$$= -\frac{F^2(\phi_i^w) \int_{\phi_i^w}^{\phi_r} \partial_k^2 \Delta\varepsilon_{cv}(k_l, \phi, \phi_i^w) d\phi}{\omega_0 \partial F(\phi_i^w)/\partial \phi_i^w}, \tag{5}$$

where ϕ_i^w and ϕ_r represent the electric field phase at the times of ionization and emission, respectively. The recollision condition in CSPM reads as

$$\int_{\phi_i^c}^{\phi_r} \partial_k \Delta\varepsilon_{cv}(k_l, \phi, \phi_i^c) d\phi = 0, \tag{6}$$

where ϕ_i^c represents the electric field phase at the time of ionization. For the same emission time, Eqs. (5) and (6) can
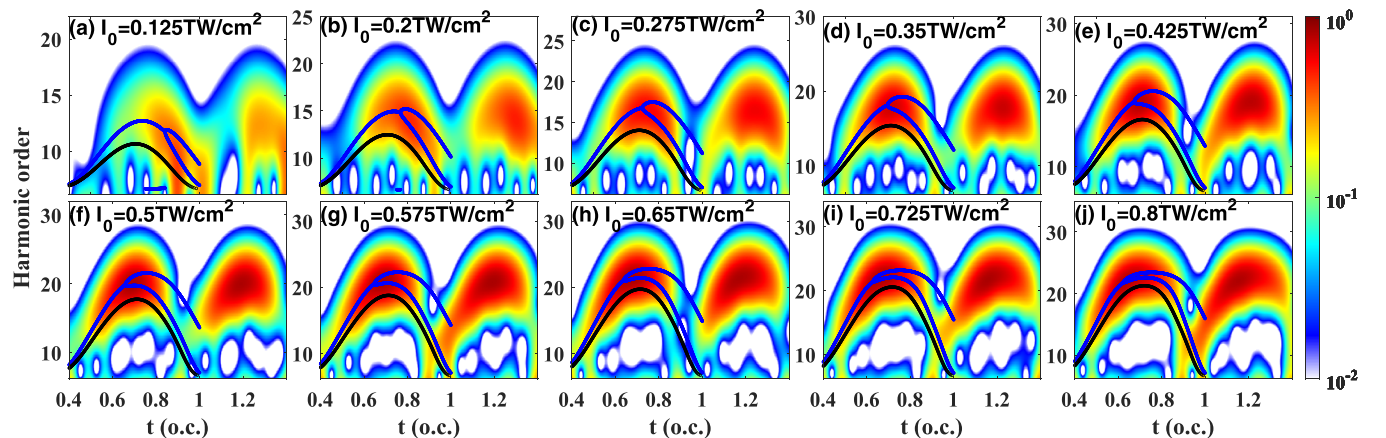

FIG. 4. The time-frequency profiles for the same wavelength 2.5 μm and varying optical intensity from 0.125 to 0.8 TW/cm². The emission channels predicted by the CSPM and WSPM are displayed with black and blue lines, respectively.
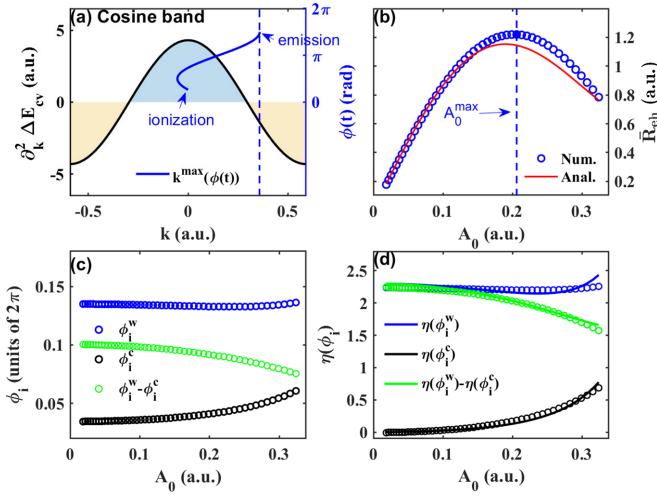
FIG. 5. (a) The second derivative of cosine band (black line). (b) The numerical (blue circle line) and analytic (red solid line) electron-hole distance $\bar{R}_{eh}$ with respect to laser vector potential A_0. The maximum of $\bar{R}_{eh}$ is marked with a dashed blue line where $A_0^{max} \approx 0.2$ a.u.. The corresponding reciprocal space trajectory $k^{max}[\phi(t)] = k_l + A_0^{max}[\phi(t)] - A_0^{max}(\phi_i)$ is displayed in (a) with blue line. (c) Ionization phase ϕ_i with respect to A_0 solved numerically with CSPM (black circle line) and WSPM (blue circle line). (d) Numerical (circle line) and analytic (solid line) $\eta(\phi_i)$ with respect to A_0.

determine different ionization phases, which correspond to different HHG processes. This difference is caused by the nonzero term on the right-hand side of Eq. (5), which represents the cycle-averaged electron-hole distance. We denote this term as $\bar{R}_w(\phi_i^w, \phi_r, A_0)$.

To reveal how the GVD leads to the parameter-dependent deviation, we then discuss the relation between $\bar{R}_w(\phi_i^w, \phi_r, A_0)$ and laser parameters. For parameters in the discussed region, the cutoff energy mostly lies on or near the time $t_r = 0.75T_0$, which corresponds to electric field phase $\phi_r = 3\pi/2$. Therefore, we solve the equations at the fixed emission phase. The details of solutions can be seen in Appendix C. The term $\bar{R}_w(\phi_i^w, \phi_r, A_0)$ can be approximately represented by the zeroth term in the Fourier expansions:

$$\bar{R}_{eh} \sim a_0 A_0 J_0^2(a_0 A_0)(\phi_r - \phi_i^w). \tag{7}$$

The analytic electron-hole distance is depicted in Fig. 5(b) with solid red line, which is consistent with the numerical result (blue circle line). From Fig. 5(b), one can see that the electron-hole distance first increases and reaches a maximum near $A_0^{max} \approx 0.2$ a.u., and then decreases with further increasing the vector potential. The reciprocal trajectory for $A_0 = A_0^{max}$ is displayed in Fig. 5(a) with blue line. One can see the whole trajectory slightly exceeds the boundary of zone with positive GVD [blue area in Fig. 5(a)]. This suggests that the electrons and holes undergo a reciprocal space motion in the Brillouin zone with positive GVD for $A_0 < A_0^{max}$. Therefore, the accumulation of GVD increases with the laser vector potential below A_0^{max}. For $A_0 > A_0^{max}$, electrons and holes can reach the Brillouin zone with negative GVD [yellow area in Fig. 5(a)]. Here, a dispersion compensation is achieved, resulting in a subsequent decrease with A_0. Apparently, due to the neglect of the parameter-dependent electron-hole

distance $\bar{R}_{eh}$, the discrepancy of ionization phases determined by WSPM and CSPM, i.e., $\phi_i^w - \phi_i^c$, is also dependent on the laser parameters. To validate this, we numerically solve Eqs. (5) and (6), the solutions of ionization phases for CSPM $[\phi_i^c(A_0)]$ and WSPM $[\phi_i^w(A_0)]$ are shown in Fig. 5(c) with black and blue circle lines, respectively. One can see that there is a large difference between them. Simultaneously, $\phi_i^c(A_0)$ increases noticeably with A_0, while $\phi_i^w(A_0)$ changes slowly with A_0. To comprehend this phenomenon, we further analytically solve Eqs. (5) and (6) in Appendix C. The analytic solution of ionization phases, which includes the dominant term, is presented below:

$$\eta\big[\phi_i^w(A_0)\big] \sim \frac{a_0 A_0 J_0(a_0 A_0)}{J_1(a_0 A_0)}, \tag{8a}$$

$$\eta\big[\phi_i^c(A_0)\big] \sim \frac{J_2(a_0 A_0)}{J_0(a_0 A_0)}. \tag{8b}$$

Here, η is a defined function representing the relative value of the ionization phase. Evidently, Eqs. (8a) and (8b) follow different dependence on A_0. As depicted in Fig. 5(d), the analytic solutions (represented by solid lines) are consistent with the numerical results (represented by circle lines). Note that the analytic results in Fig. 5 include the Fourier series up to the third order. From Eqs. (5), (7), and (8a), we can know that the electron-hole distance related to the GVD remains roughly synchronized with the classical displacement across different parameters. This synchronization keeps the ionization phases of WSPM to be roughly the same for different parameters. Differently, without the synchronization, the ionization phases for CSPM are significantly dependent on the laser parameters. Overall, the discrepancy of ionization phase between the CSPM and WSPM is more significant for small laser vector potentials [as shown with green lines in Fig. 5(d)].

Finally, we will explain how such a difference in HHG process can manifest in the relative deviation of cutoff energy as shown in Figs. 3(d) and 4. The difference of cutoff energy between the WSPM and CSPM can also be expressed as an expansion of Fourier series:

$$\Delta E^{cut}(A_0) \sim 2J_0(a_0 A_0)J_2(a_0 A_0)\big[\cos(\phi_i^w) - \cos(\phi_i^c)\big]$$
$$- 4J_1^2(a_0 A_0)\big[\sin(\phi_i^w) - \sin(\phi_i^c)\big]$$
$$+ \cdots. \tag{9}$$

Apparently, the deviation is contributed by two parts: the Bessel coefficients and the difference of ionization phase. The former originates from the nonlinearity of the energy band, which determines the absolute deviation of the cutoff energy as shown in Fig. 3(b). Removing the contribution of the nonlinearity of energy band, the relative deviation is determined by the difference of ionization phase. Evidently, in Figs. 3(d) and 4, the more significant relative deviation for small vector potential is attributed to larger difference of ionization phase [green lines in Fig. 5(d)].

III. WAVELIKE DYNAMICS IN GAPPED GRAPHENE

A. Systems with different band gaps

In the previous discussion, we analyzed the wavelike dynamics in a simple one-dimensional (1D) system. Here,
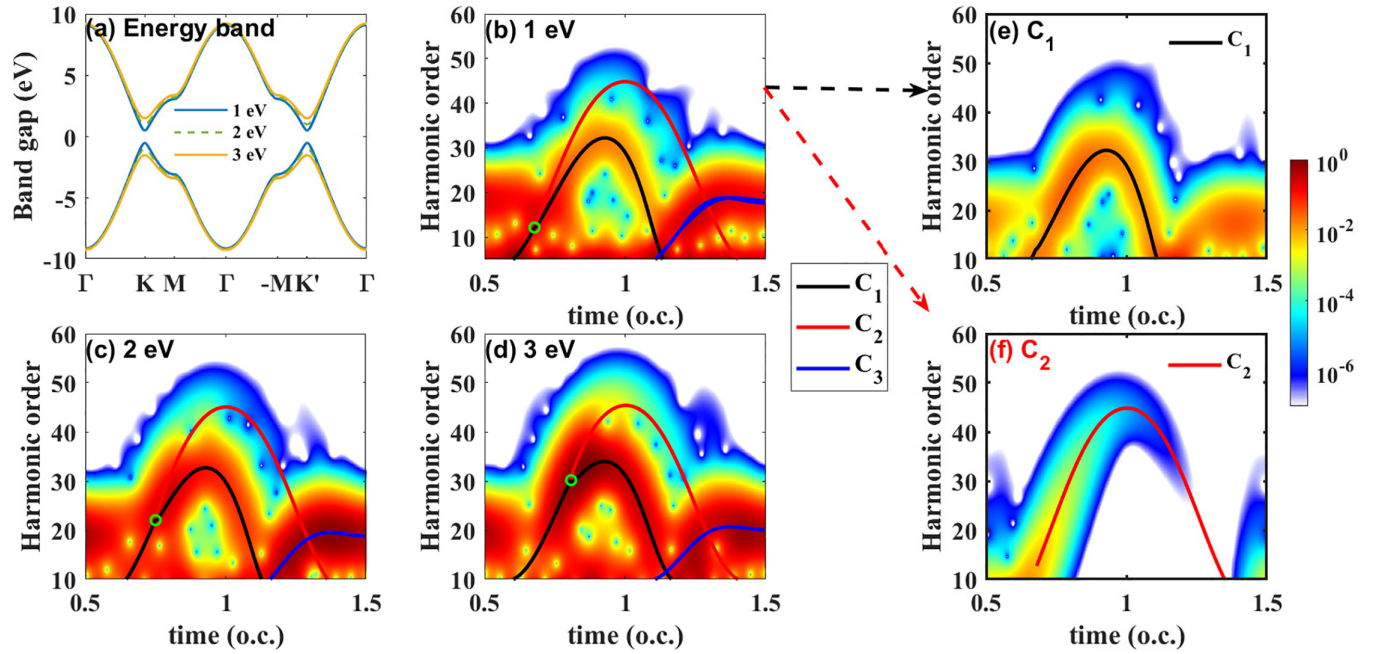
FIG. 6. (a) The energy band with different band gaps along the high-symmetry directions. The time-frequency profiles and the emission channels predicted by WSPM for different band gaps: 1 eV (b), 2 eV (c), and 3 eV (d). For 1-eV band-gap case, the contributions of channels C_1 and C_2 to the total time-frequency properties are separated, and shown in (e) and (f), respectively.

we will further take the gapped graphene as an example to illustrate the wide applicability of our analyzation. Gapped graphene is a model system, which can be used to mimic different 2D materials by adjusting the band gap and hopping parameters. As shown in Fig. 6(a), the gapped graphene has two nonequivalent valleys, K and K' valleys, with opposite Berry curvature but symmetric energy band. For simplicity, we only analyze the time-domain interference for the contributions of a single ionization momentum $\mathbf{k}_l = \mathbf{K}$. For noncentrosymmetric crystals, the classical action is formulated as $S(\mathbf{k}', t, t') = \int_{t'}^{t} \Delta\varepsilon_{cv}[\mathbf{k}(\mathbf{k}', \tau, t')] + \mathbf{F}(\tau) \cdot (\mathbf{X}_{cc} - \mathbf{X}_{vv})d\tau - \phi_{cv}(\mathbf{k}', t, t') + \phi_{cv}(\mathbf{k}', t')$. Here, $\mathbf{k}(\mathbf{k}', \tau, t') = \mathbf{k}' + \mathbf{A}(\tau) - \mathbf{A}(t')$. The second term in this formula is the Berry phase with $\mathbf{X}_{cc}$ and $\mathbf{X}_{vv}$ the Berry connections [34,35]. The last two terms are the phases of transition dipole. Both of them vanish in symmetric materials. Similarly, the condition of slow-varying phase becomes

$$|\partial_{t'}S| = |\Delta\varepsilon_{cv}(\mathbf{k}_l) - \mathbf{F}(t') \cdot \{\mathbf{x}[\mathbf{k}(t)] - \mathbf{R}_{cv}[k(t)]\}|. \quad (10)$$

Here, $\mathbf{R}_{cv}$ represents the shift vector, which is defined based on both the Berry connection and the dipole phase [36]. The basic form of Eq. (10) keeps consistent with Eq. (2), except for the additional electron-hole displacement contributed by the shift vector. For 2D systems, the shift vectors are distinct for the components of emission along different directions. Therefore, one should consider the emission along different directions individually. Usually, the shift vector is far smaller than the classical displacement contributed by the dynamical phase.

Using Eq. (10), we examine the validation of WSPM across three distinct band gaps: 1 eV [Fig. 6(b)], 2 eV [Fig. 6(c)], and 3 eV [Fig. 6(d)]. For the three band gaps, we employ a same mid-infrared laser linearly polarized along the Γ-K direction with field parameters of 0.4 TW/cm^2, 3.8 μm, and solve the

SBEs as used in graphenelike systems [37–40]. We note that the vertical component is dominant for total interband emission, and thus we mainly focus on the vertical component. All the emission channels within one full cycle determined by Eq. (10) are represented with the solid lines, and numbered as C_1 (black), C_2 (red), and C_3 (blue) in accordance with the emission time when they first appear. We note that C_1 and C_2 denote the emission channels in the first half-cycle (about 0.5~1 o.c.), C_3 denotes all the emission channels in the later half-cycle (about 1~1.5 o.c.). Due to the asymmetry of energy band in the Γ-K direction, the emission structures in two adjacent half-cycles are different. Besides, the signal of channel C_2 is much weaker than that of C_1, and not easy to be distinguished. For clarity, we separate the total signal for the case of 1-eV band gap into the contributions from C_1 [Fig. 6(e)] and C_2 [Fig. 6(f)] according to their different ionization time. One can see that C_1, C_2, and C_3 are all in good agreement with the SBEs simulations. This implies that the WSPM is applicable for materials with different band gaps. Additionally, we mention two unique phenomena here. On the one hand, the channel C_2 occurs after the time t_s (marked with green circles), and the intensity of C_2 is three to five orders of magnitude lower than that of C_1. On the other hand, the emission of long orbit is enhanced as the increase of band gaps. We will discuss these questions in detail in the following section.

B. Emission intensity analysis based on the interference principle

To highlight the importance of the wavelike dynamics in HHG process, we further unravel the interference process embedded in the intensity of HHG emission. In Eq. (1), the harmonic yield is dependent on both the time-domain and

momentum interferences. Considering the dominant role of the time-domain interference, we just analyze the emission contributed by a single ionization momentum k_l, it solely depends on the time-domain interference:

$$Y_{\mathbf{k}_l}(\Omega, t_r) \propto \left| \sum_{t' \in [0, t_r]} f(\mathbf{k}_l, t') P(\mathbf{k}_l, t_r, t') e^{-iS(\mathbf{k}_l, t_r, t')} \right|^2, \quad (11)$$

where $P(\mathbf{k}_l, t_r, t') = G[\partial_{\mathbf{k}'} S(\mathbf{k}_l, t_r, t'), \Delta x] W[\partial_t S(\mathbf{k}_l, t_r, t') - \Omega, \Delta E] D_{vc}(\mathbf{k}_l, t_r, t')$ describes the emission amplitude of a single wavelet, with G and W two Gaussian functions, and D_{vc} is the emission dipole. One can see that the emission intensity is determined by several factors, which represent the contributions from different HHG processes.

(i) The first term $f(\mathbf{k}_l, t')$ is the expansion coefficients in Gaussian basis, which is proportional to the field strength $F(t')$ and transition dipole $\mathbf{X}_{cv}(k_l)$. It describes the amplitude of a wavelet ionized at t'. For a specific ionization channel $\mathbf{k}_l$, it depends solely on the field strength $\mathbf{F}(t')$.

(ii) The second term, $G[\partial_{\mathbf{k}'} S(\mathbf{k}_l, t_r, t'), \Delta x] = k_w \sqrt{\pi} \exp\{-[\partial_{\mathbf{k}'} S(\mathbf{k}_l, t_r, t')/\Delta x)]^2\}$, describes the interference of wavelets in k' space. Here, $\partial_{\mathbf{k}'} S(\mathbf{k}_l, t_r, t') = \mathbf{x}(\mathbf{k}_l, t_r, t') - \mathbf{R}_{cv}(\mathbf{k}_l, t_r, t')$ is the distance of electron-hole pair at the observation time t_r, which represents the rate of phase change along k' direction. $\Delta x = 2/k_w$ with k_w the width of reciprocal-space Gaussian wavelets, and we use $k_w = 0.01 \frac{\pi}{a_0}$. This term implies that the emission intensity decreases exponentially with the electron-hole distance.

(iii) The third term, $W[\partial_t S(\mathbf{k}_l, t_r, t') - \Omega, \Delta E] = t_w \sqrt{\pi} \exp\{-[(\partial_t S(\mathbf{k}_l, t_r, t') - \Omega)/(\Delta E)]^2\}$, describes the emission intensity of the observed frequency Ω. Here, $\partial_t S(k_l, t_r, t') = \Delta \varepsilon_{cv}(\mathbf{k}_l, t_r, t') + \mathbf{F}(t_r) \cdot \mathbf{R}_{cv}(\mathbf{k}_l, t_r, t')$ represents the emission frequency of a wavelet. Similarly, this term suggests that the emission intensity of the observed frequency Ω decreases exponentially as the deviation from the most probable frequency $\Omega_c = \Delta \varepsilon_{cv}(\mathbf{k}_l, t_r, t_i) + \mathbf{F}(t_r) \cdot \mathbf{R}_{cv}(\mathbf{k}_l, t_r, t_i)$.

(iv) $\mathbf{D}_{vc}(\mathbf{k}_l, t_r, t') = \Delta \varepsilon_{vc}(\mathbf{k}_l, t_r, t') \mathbf{X}_{vc}(\mathbf{k}_l, t_r, t')$ represents the emission dipole, which describes the probability of emission. There is no variation in order of magnitudes throughout the entire Brillouin zone for the emission dipole.

(v) The factors mentioned above determine the emission amplitude of each independent wavelet. However, the final yield is determined by the interference of these wavelets, which also depends on their phases. According to Eq. (10), we can determine the most probable ionization time t_i. This means that the constructive interference of wavelets ionized near t_i will contribute primarily to the HHG emission. We consider the wavelets ionized within the interval $[t_i - \Delta t, t_i + \Delta t]$. The amplitudes for these wavelets can be considered as a constant quantity $I_0(t_i)$ due to its much slower variation compared to phase. In this context, the integral in Eq. (11) can be approximately calculated with a Gaussian integral:

$$I_0(t_i) \int_{-\infty}^{+\infty} dt' \exp\left[-\frac{1}{2} g_0 (t' - t_i)^2 - iS(k_l, t_r, t') \right], \quad (12)$$

where $g_0 = \frac{2\ln 2}{\Delta t^2}$ describe the width of Gaussian function, and $\Delta t = 0.04 T_0$ is used here. We denote the integral term as the interference factor $\zeta(k_l, t_i, t_r)$. By expanding the phase
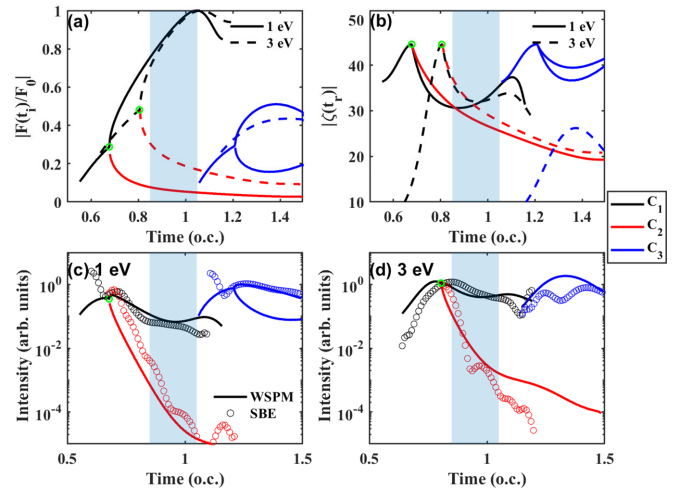

FIG. 7. (a) The normalized field strength at the ionization time for two band gaps: 1-eV (solid lines) and 3-eV band gaps (dashed lines). The color of lines indicates different channels: C_1 (black), C_2 (red), C_3 (blue). (b) The interference factor with respect to emission time t_r. (c), (d) The total emission intensity calculated with Eq. (14) for 1- and 3-eV band gaps, respectively.

to the second order $S(t') = S(t_i) + S'_{t'}|_{t_i}(t' - t_i) + \frac{1}{2} S''_{t'}|_{t_i}(t' - t_i)^2$, the interference factor can be easily obtained:

$$\zeta = \int_{-\infty}^{+\infty} \exp\left[-\frac{1}{2}(g_0 + iS''_{t'})(t' - t_i)^2 - iS'_{t'}(t' - t_i) \right] dt'$$

$$= \sqrt{\frac{2\pi}{g_0 + iS''_{t'}}} \exp\left[-\frac{S'^2_{t'}}{2(g_0 + iS''_{t'})} \right]. \quad (13)$$

The interference factor has negative correlation with the rate of phase change.

(vi) Additionally, the dephasing effect can influence the intensity of HHG emission, which can be represented by the factor $D_p = \exp(-\frac{t_r - t_i}{T_2})$. Here, the dephasing time T_2 is set to 5 fs as commonly used in graphenelike materials [29,41,42].

In summary, the factors mentioned above collectively determine the ultimate emission intensity. Overall, the time-domain relative intensity for the center frequency Ω_c can be approximated as follows:

$$Y_{\mathbf{k_l}}(\Omega_c, t_r) \propto |\mathbf{F}(t_i) \cdot \mathbf{X}_{cv}(k_l) \mathbf{D}_{vc}(t_r) G \zeta(k_l, t_r, t_i) D_p|^2. \quad (14)$$

The general intensity picture can provide a comprehensive understanding of the HHG process, including the ionization, emission, and time-domain interference, all of which can affect the emission intensity.

Then, we discuss the phenomena mentioned in the prior section, i.e., the significant difference in intensity of HHG emission between C_1 and C_2, and the enhanced intensity of long-orbit HHG emission for larger band gaps. We will show how one can understand these phenomena, and unravel the underlying electronic dynamics from the perspective of wave-like picture. For simplicity, we only consider the results in the cases of 1- and 3-eV band gaps in Figs. 6(b) and 6(d). Figure 7(a) presents the normalized ionization amplitudes of three channels C_1 (black lines), C_2 (red lines), and C_3 (blue lines) for 1-eV (solid lines) and 3-eV (dashed lines) cases,

respectively. Apparently, C_1 has a larger ionization amplitude than C_2. Additionally, the interference factor with respect to emission time t_r is shown in Fig. 7(b). It has a maximum at the temporal position t_s (marked with green circles) where both of $S''_{t'}$ and $S''_{t'}$ equal to zero. The ultimate emission intensity is calculated with Eq. (14), and displayed in Figs. 7(c) and 7(d) for 1- and 3-eV cases, respectively. The emission intensity for the results of SBEs in Figs. 7(c) and 7(d) is directly extracted from the time-frequency data along the emission channels in Figs. 6(b) and 6(d). This is equivalent to Gabor transformation of the interband currents at the temporal position t_r for the central emission frequency $\Omega_c(t_r)$, both of which are determined by WSPM. Overall, one can see that the emission intensity predicted by WSPM is consistent with the results of SBEs (circle lines) qualitatively. It is worth to note that the intensity of C_1 is always dominant and several orders higher than that of C_2. This is mainly ascribed to their significant discrepancy in ionization amplitudes. In addition, we also compare the emission intensity of 1- and 3-eV cases near the time emitting the cutoff energy, i.e., the shadow region. The intensity of the 1-eV case is significantly weaker than that of the 3-eV case. For the 1-eV case, the interference factor has attenuated to a minimal value due to a larger interval between this region and t_s. Whereas the interference factor is relatively larger for the 3-eV case due to a smaller interval between this region and t_s. Clearly, the time-domain interference of wavelets will affect the intensity of HHG emission, and leads to significant difference of long-orbit emission for 1- and 3-eV cases.

C. Revealing the 2D electronic dynamics from the perspective of particlelike trajectory

Previously, 2D electronic dynamics were rarely explored due to the limitations of the CSPM. For instance, meeting the recollision condition was difficult when driven by a 2D elliptically polarized light [31,32]. Considering the limitation of CSPM in 2D cases, it is necessary to adopt an extended recollision model in which the electrons and holes do not need to reencounter exactly. Usually, it is referred to as electron-hole imperfect recollision (ehIR). Here, we will revisit these issues from the perspective of wavelike picture. Following the same procedure as in the 1D case, the WSPM can also be applied to describe the HHG emission in full Brillouin zone for 2D cases. Detailed explanations are provided in Appendix A. For simplicity, we only consider the emission in the entire K valley of gapped graphene with a band gap of 3 eV at K point. We employ a 2D elliptically polarized light: $\mathbf{F}(t) = \frac{\epsilon F_0}{\sqrt{1+\epsilon^2}}\cos(\omega_0 t)\vec{\mathbf{e}}_x + \frac{F_0}{\sqrt{1+\epsilon^2}}\sin(\omega_0 t)\vec{\mathbf{e}}_y$, where ϵ is the ellipticity, and the field strength and frequency are $F_0 = 0.0065$ a.u. and $w_0 = 0.015$ a.u. The time-frequency properties are shown in Fig. 8 for two different ellipticities: 0.5 [Fig. 8(a)] and 1 [Fig. 8(b)]. For the elliptically polarized lights, there are three emission structures within one cycle due to the threefold rotational symmetry of energy band. The emission channels predicted by WSPM are displayed with black lines. One can see that they are in good agreement with SBEs simulations. Undoubtedly, the WSPM is also applicable for 2D systems.

It seems that there is a commonality between the WSPM and ehIR, i.e., the electrons and holes are all separated spatially when emitting HHG. In fact, these two
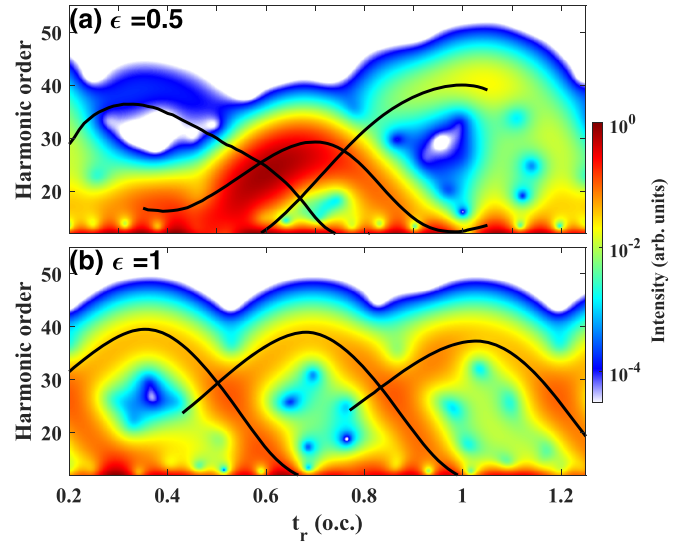

FIG. 8. The time-frequency profiles contributed by the full K valley driven by elliptically polarized light with different ellipticities: (a) $\epsilon = 0.5$, (b) $\epsilon = 1$. The black lines show the central emission frequency predicted by the WSPM.

models are essentially different. To illustrate their difference, we further explore the electronic dynamics of 2D systems by comparing the real-space electron-hole trajectories determined by the ehIR and WSPM. For generality, we adopt a 2D orthogonally polarized two-color field (OTC): $\mathbf{F}(t) = F_0[\sin(\omega_0 t)\vec{\mathbf{e}}_x + \cos(2\omega_0 t)\vec{\mathbf{e}}_y]$, with field strength and frequency are $F_0 = 0.0048$ a.u. and $\omega_0 = 0.0152$ a.u., respectively. The initial ionization momentum is chosen as $k_l = \mathbf{M}$ where the band gap is 7.26 eV. In this context, both of laser vector potential and energy band are symmetric with respect to x (Γ-M) and y (K-M) directions, thereby facilitating the imperfect recollision events. The time-frequency property simulated with SBEs is shown in Fig. 9(a). For the OTC field, the exact recollision rarely occurs, and thus we adopt the ehIR, and relax the restriction of recollision distance to 10 a_0 (a_0 is the lattice constant). The emission channel predicted by ehIR is shown with black lines. One can see that it deviates significantly from the SBEs simulation in both emission time and energy. In contrast, the prediction of WSPM (blue lines) agrees well with SBEs simulations. This means that the ehIR also fails to describe the 2D electronic dynamics in HHG process.

To unravel the basic difference underlying these two perspectives we focus on the electron-hole particlelike trajectories. In Fig. 9(a), we consider the emission of 30th harmonics (marked with dashed white line). For WSPM, the emission times are marked with green dots A_1 and A_2 for short and long orbits, respectively. Similarly, the emission times for ehIR are also marked with the red dots B_1 and B_2. The corresponding real-space trajectories of electrons (solid lines) and holes (dashed lines) are shown in Figs. 9(b) and 9(e) with the position at the emission time marked with dots (electrons) and circles (holes). For clarity, the straight-line distances $|R_{eh}(t)|$ of electron-hole pairs are also shown in Figs. 9(c) and 9(f) correspondingly, with the emission times marked with dots. It is evident that electrons and holes undergo entirely
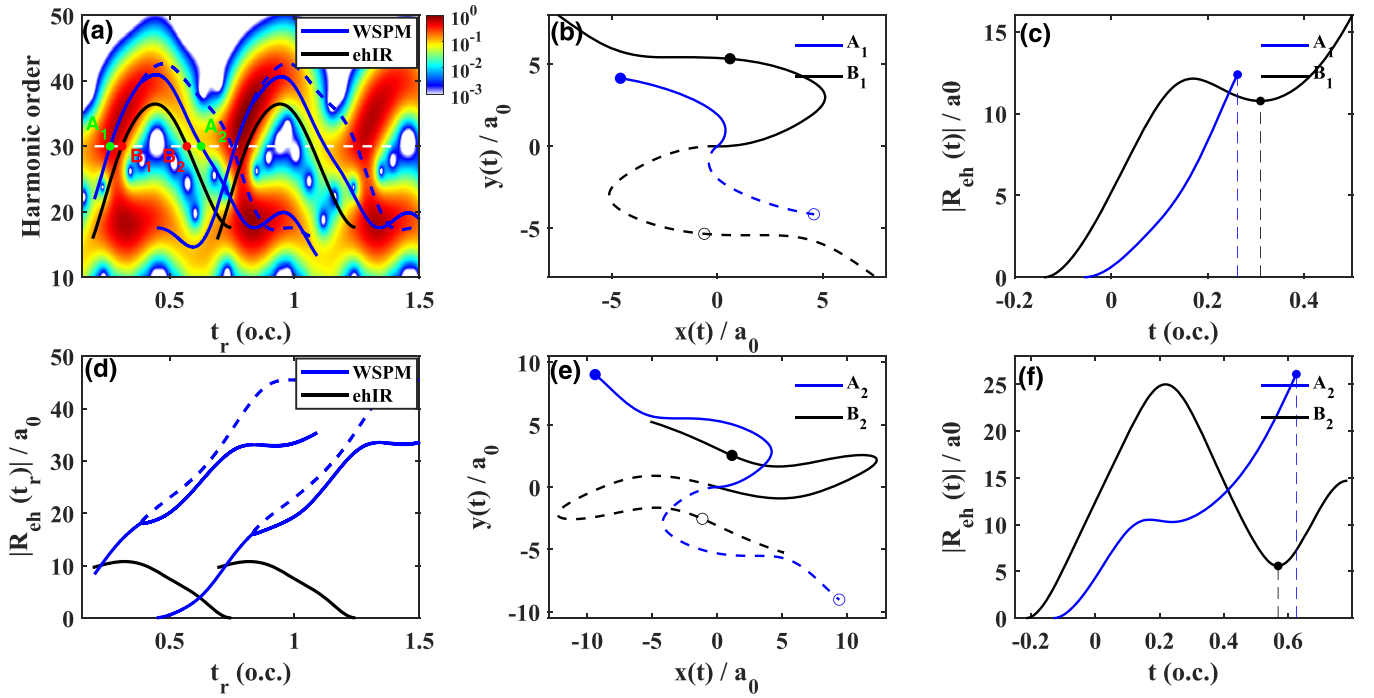
FIG. 9. (a) The time-frequency profile contributed by momentum $k_l = M$ driven by an orthogonally polarized two-color field. The emission channels determined by WSPM and ehIR are shown with blue and black lines, respectively. The 30 order harmonic is marked by a dashed white line, with corresponding emission time marked with red or green dots: A_1, A_2 and B_1, B_2. The real-space trajectories of electrons and holes are exhibited for points A_1, B_1 (b) and A_2, B_2 (e), respectively, with the emission position marked with filled dots (electron) or circles (hole). The time-dependent straight-line distances between the electron and hole pairs for A_1, B_1 (c) and A_2, B_2 (f). (d) The emission distances of all other electron-hole pairs which emit HHG at different time t_r.

different movement in real space for WSPM and ehIR. For ehIR, the emission probability depends on the electron-hole distance, reaching a maximum when they are spatially closest. In contrast, the emission probability for WSPM is largely independent of the electron-hole distance. Furthermore, The emission distances of all other electron-hole pairs which emit HHG at different time t_r are shown in Fig. 9(d) for WSPM (blue line) and ehIR (black line), respectively. One can see that they follow completely different trends. This indicates that the criteria of ehIR, which are based only on particlelike trajectories, are not reliable. To better quantify the HHG process, it is necessary to take into account the interference of wavelets.

IV. CONCLUSION

To summarize, the wavelike dynamics in solid-state HHG was studied. In solids, the GVD arising from the nonquadratic energy band can lead to substantial spatial spread for the evolution of electron wave packet. This kind of wavelike effect can also significantly affect the electronic dynamics of HHG emission, and allows the electrons and holes to be separated spatially when emitting HHG. Incorporating the wavelike effect, the time-frequency properties of HHG emission and the underlying dynamics can be well understood by the wavelike picture. Furthermore, the wavelike picture is also demonstrated to be able to describe the 2D electronic dynamics and emission intensity. Our analysis has provided a comprehensive understanding on the HHG emission properties, as well as the underlying electronic dynamics.

APPENDIX A: INTERFERENCE ANALYSIS IN WSPM

According to Eq. (1), the harmonic yield is determined by both the time-domain t' and momentum space k_l interference. The results of interference are related to the rate of phase change, which can be described by the partial derivative of S with respect to t' and k_l:

$$|\partial_{t'} S| = |\Delta\varepsilon_{cv}(k_l) - x(k_l, t_r, t')F(t')|, \quad \text{(A1a)}$$

$$|\partial_{k_l} S| = |x(k_l, t_r, t')|. \quad \text{(A1b)}$$

In general, $|\partial_{t'} S|$ is much smaller than $|\partial_{k_l} S|$, and the integration domain of t' (same order of magnitude as T_0, about 10^2 a.u.) is much larger than that of k_l (same order of magnitude as $2\pi/a_0$, about 10^0 a.u.). These factors result in the time-domain interference playing a dominant role in Eq. (1). Therefore, we can tackle the time-domain integral in Eq. (1) exactly for each single ionization momentum k_l independently, while taking an approximate treatment for the integral of k_l. Figure 10(a) displays the value of Eq. (A1a) with respect
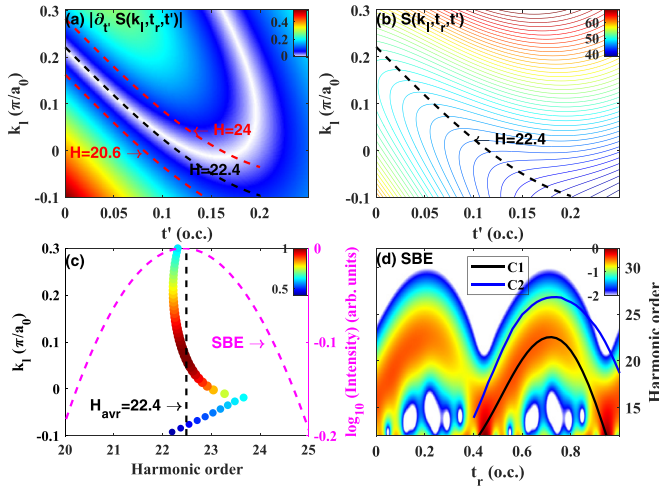
FIG. 10. (a) The value of Eq. (A1a) with respect k_l and t' for $t_r = 0.7\,T_0$. The dashed lines indicate the k_l and t' which correspond to the same harmonic order. (b) The contour lines for the classical action $S(k_l, t_r, t')$ at $t_r = 0.7\,T_0$. (c) The colored scatter plot shows the most probable emission frequency for different ionization momentum k_l with the color indicating the normalized amplitude $f(k_l, t_i)$. The dashed black line marks the weighted average frequency. The dashed magenta line shows the intensity distribution of SBEs simulation. (d) The time-frequency properties simulated with SBEs. The solid lines show the emission channels predicted by WSPM.
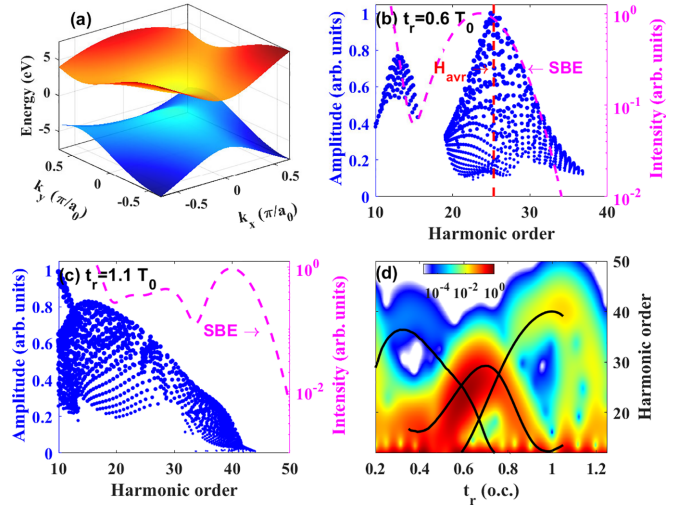

FIG. 11. (a) The energy band of gapped graphene in the K valley, and the K point is shifted to the zero point for clarity. (b) The blue dots represent the frequency-domain emission distribution (emission frequencies and the corresponding normalized amplitudes) of the different ionization momenta k_l for $t_r = 0.6\,T_0$. The dashed magenta line shows the emission intensity calculated by SBEs. (c) Same as (b), but for $t_r = 1.1\,T_0$. (d) The time-frequency properties simulated by SBEs. The black lines show the emission channels predicted by WSPM.

to t' and k_l for $t_r = 0.7\,T_0$. It can be seen that the minima for each k_l are distributed within a narrow range between two dashed red lines, which corresponds to emission frequency range: $20.6\,\omega_0 \sim 24\,\omega_0$. Most of them are near the frequency $22.4\,w_0$, as marked with the dashed black line. For clarity, we present a contour plot of the classical action $S(k_l, t_r, t')$ in Fig. 10(b). It can be seen that $S(k_l, t_r, t')$ is flat along the t' direction for the frequency $22.4\,\omega_0$. This implies that the most probable emission frequencies for electrons ionized from different momenta are very close. In Fig. 10(c), the distribution of the most probable emission frequency for each k_l, i.e., $H(k_l)$, is shown with colored scatter dots. The color of the dots indicates the normalized amplitude of electron-hole wavelets, i.e., $f(k_l, t_i) = |d_{cv}(k_l)F(t_i)|$. Consequently, the central emission frequency after the interference of the contribution from all ionization momenta can be approximately represented by the weighted average frequency:

$$H_{\text{avr}} = \frac{1}{\sum_{k_l} f(k_l)} \sum_{k_l} f(k_l) H(k_l). \tag{A2}$$

The average frequency is plotted with a dashed black line. One can see that it agrees well with the SBEs simulations as shown with the dashed magenta line. It is worth to note that the average frequency is artificially defined to describe the whole distribution of emission frequencies, and only suitable for a concentrated distribution. Figure 10(d) displays the predicted central emission frequency within half of optical cycle. One can see that the channel C1 aligns well with the SBEs simulation. In addition, we also present the second channel C2, which corresponds to the second minimum of $\partial_{t'}S$ [seen in Fig. 10(a)]. However, the value of Eq. (A1b)

for C2 is large, indicating a fast-changing phase along the k_l direction [seen in Fig. 10(b)]. Therefore, for channel C2, the interference between different ionization momenta is destructive. Moreover, ionization amplitude $F(t_i)$ for C2 is close to zero. As a result, C2 is significantly weaker than C1, and thus we pay less attention to C2.

The analysis above is also applicable to the 2D case. In the 1D case, we can easily estimate the relative amplitudes of wavelets contributed to two distinct channels, C1 and C2, and discuss them individually. However, this is challenging for the 2D case. In this context, using only $f(k_l, t_i)$ to describe the amplitudes may overestimate the contribution of some wavelets. To be precise, we adopt a more precise expression for the amplitude of the wavelets after time-domain interference, i.e., Eq. (14).

For simplicity, we only consider the emission in the K valley of the gapped graphene excited by an elliptically polarized light with an ellipticity $\epsilon = 0.5$. The energy band with a band gap of 3 eV is shown in Fig. 11(a). Similar to the 1D case, we can determine the most probable emission frequency for each individual momentum $\mathbf{k}_l = [k_x, k_y]$, as well as the corresponding amplitude. By aggregating the contributions from all momenta, we can obtain the frequency-domain distribution of all possible emissions, as shown in Figs. 11(b) ($t_r = 0.6\,T_0$) and 11(c) ($t_r = 1.1\,T_0$) with a blue scatter plot. For $t_r = 0.6\,T_0$, most of the emission is distributed within a narrow range (about $20 \sim 30$ order) with a center frequency of $25.3\,\omega_0$. This agrees with the narrow peak in the emission distribution of SBEs simulations as shown with dashed magenta line. For $t_r = 1.1\,T_0$, a wider distribution within about $10 \sim 40$ order can account for a wide-band emission simulated with SBEs (dashed magenta line). In this context, an weighted average

frequency is not suitable to represent the character of emission anymore, so we do not show the center frequency for the interval 1 $T_0 \sim 1.2\ T0$. Overall, The WSPM is valid for both 1D and 2D systems.

APPENDIX B: INFLUENCE OF GVD ON WAVE PACKET DYNAMICS IN SOLIDS

Here, we discuss the effect of higher derivatives of energy band on the wave-packet evolution in solids. It has been found that the electron wave packet propagating in solids can undergo significant changes in spatial width and waveform, as seen in the supplementary materials of the references [29,30]. While the underlying dynamics for the wave-packet evolution remains unclear. We aim to provide a general physical picture to establish the relationship between the wave-packet dynamics and the electronic structure of solids. To begin, we also construct a real-space Gaussian wave packet, and the evolution of the wave packet can be described by the formula

$$\Psi(x, t, t_0) = \int_{-\infty}^{\infty} dk\, g(k) e^{ikx - i\varphi(k, t, t_0)}. \quad (B1)$$

Here, $g(k) = e^{-(k-k_0)^2/2\alpha^2}$ represents an initial Gaussian wave packet with the center at k_0. $\varphi(k, t, t_0)$ is the classical action accumulated within the temporal interval $[t_0, t]$. To theoretically obtain the dynamical properties of the electron wave packet, we consider a narrow wave packet. Consequently, the

classical action can be Taylor expanded at the center of the wave packet k_0:

$$\varphi(k) = \sum_{n=0}^{3} \frac{\varphi^n(k_0)}{n!} (k - k_0)^n + O((k - k_0)^4). \quad (B2)$$

We denote $x_c = (d\varphi/dk)_{k_0}$, which corresponds to the accumulation of the group velocity of the wave packet, i.e., the classical displacement. $\beta = (d^2\varphi/dk^2)_{k_0}$ and $\gamma = (d^3\varphi/dk^3)_{k_0}$ represent the accumulation of the second and third derivatives of energy band, respectively. The second derivative is usually called the group velocity dispersion (GVD), while the third derivative of energy band is called group delay dispersion (GDD). We retain only the lowest three orders and rewrite the integral in Eq. (B1) by replacing $k - k_0$ with k. Then, the evolution of the wave packet can be approximately described by

$$\Psi(x, t) = \frac{e^{-i\varphi_0(t)}}{\sqrt{2\pi}} \int_{-\infty}^{+\infty} e^{ik(x - x_c) - \frac{k^2}{2}(i\beta + 1/\alpha^2)} \left[1 - \frac{i}{6}\gamma k^3 \right] dk. \quad (B3)$$

Here, the term k^3 is a small quantity for a narrow wave packet, so we have taken it out of the exponent. By simplifying the Gaussian integral above, we can obtain the time-dependent spatial density distribution of wave packet:

$$|\Psi(x, t)|^2 \approx \frac{\alpha^2}{\sqrt{1 + \beta^2 \alpha^4}} \left\{ 1 + \gamma \left[\frac{\alpha^4 (1 - \beta^2 \alpha^4)}{(1 + \beta^2 \alpha^4)^2} (x - x_c) + \frac{\alpha^6 (\beta^2 \alpha^4 - 1/3)}{(1 + \beta^2 \alpha^4)^3} (x - x_c)^3 \right] \right\} \exp \left[-\frac{\alpha^2}{1 + \beta^2 \alpha^4} (x - x_c)^2 \right]. \quad (B4)$$

Here, the higher-order terms $O[(x - x_c)^4]$ with tiny coefficients are discarded. From the formula above, we can see that the wave packet remains approximately Gaussian, with the center at the classical displacement $x_c(t)$ during propagation. Meanwhile, significant changes in the spatial distribution are characterized by a time-dependent exponent factor and a deformation factor in square brackets, which correspond to the spatial spread and deformation of the wave packet, respectively. To characterize these effects, we introduce two parameters based on Eq. (B4), namely, the full width at half-maximum (FWHM) w and the deviation Δx between the average displacement $\langle x(t) \rangle = \int_{-\infty}^{+\infty} x |\Psi(x, t)|^2 dx$ and the classical displacement x_c:

$$w \approx \frac{1}{\alpha} \sqrt{1 + \beta^2 \alpha^4} \sim \alpha \left| \int_{t_0}^{t} \partial_k^2 \varepsilon_{cv}[k(t)] dt \right|, \quad (B5a)$$

$$\Delta x = \langle x \rangle - x_c = \frac{1}{4} \alpha^2 \gamma. \quad (B5b)$$

The formulas above indicate that the width of wave packet depends on the integral of GVD, while the deformation is related to the integral of GDD. Evidently, it is insufficient to describe the wave-packet dynamics solely through the classical displacement when the effect of the GVD and GDD is significant.

To validate the discussion above, we consider a wave packet propagating on the conduction band of ZnO, and illustrate the wavelike effects caused by GVD and GDD. By numerically solving Eq. (B1), we can simulate the propagation of an electron wave packet driven by a mid-infrared laser with parameters $F_0 = 0.003$ a.u., $\omega_0 = 0.0152$ a.u. Figure 12 illustrates the time-dependent spatial distribution under three scenarios: including the full dynamical phase [Fig. 12(a)], and including the phase expanded up to the second [Fig. 12(b)] and third order [Fig. 12(c)]. The classical and average displacements of the wave packet are marked with black and dashed red lines, respectively. One can see that the wave packet's center still adheres to classical movements. Notably, the width changes significantly when including the GVD, while deformation occurs when including the GDD. Figure 12(d) further intuitively exhibits these effects through the wave-packet distribution at $t = T_0/2$. The wave packet including the GVD is a symmetric Gaussian function, while it becomes asymmetrical when including the GDD as predicted by Eq. (B4). In Figs. 12(e) and 12(f), the numerical and analytic FWHM and displacement deviation Δx of wave packet are presented with the solid blue lines and dashed red lines, respectively. Except for a minor deviation arising from the approximations made in the theoretical derivation, the numerical and analytic results are in good agreement. This demonstrates the significant influence of GVD and GDD on dynamics of
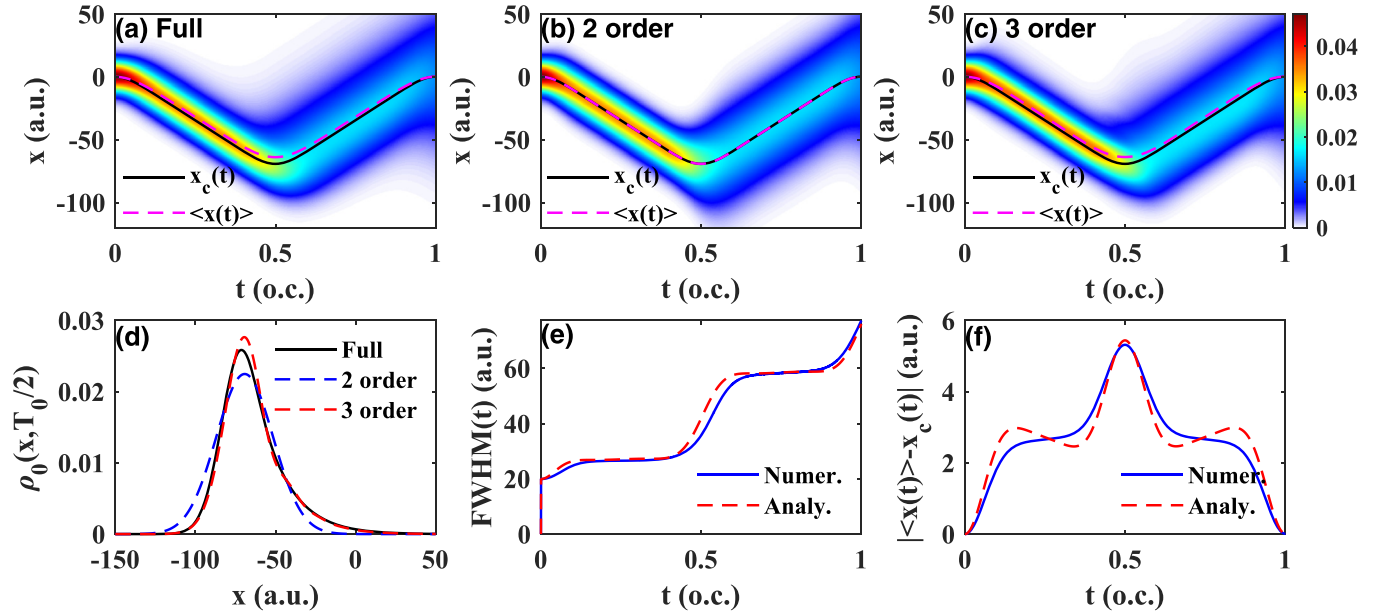
FIG. 12. (a) The propagation of a Gaussian wave packet on the conduction band, with the classical displacement and the average displacement indicated with black and dashed magenta lines. Same as (a), but Taylor expanding the dynamical phase to the second (b) and third order (c). (d) The spatial density distribution of wave packet for the three cases above at the time $t = 0.5\ T_0$. (e) The time-dependent width of wave packet obtained numerically (solid blue line) and analytically (dashed red line). (f) The time-dependent deviation of average displacement from the classical displacement obtained from numerical (solid blue line) and analytic (dashed red line) methods.

electron wave packet, suggesting that the classical movement is insufficient to fully describe the electronic dynamics in solids.

In Sec. II B, we have discussed the effect of GVD on HHG emission. Here, we will further discuss the effect of GDD by comparing the results with and without the contribution of GDD. For this purpose, we perform a calculation under the Keldysh approximation, and the interband current can be expressed as (seen in Refs. [28,30])

$$J_{\text{er}}(t) = - \int_{\text{BZ}} dk' \int_{-\infty}^{t} dt' F(t') X_{cv}(k') \Delta\varepsilon_{cv}(k', t, t')$$
$$\times X_{cv}(k', t, t') e^{-iS(k', t, t') - (t-t')/T_2} + \text{c.c.} \quad \text{(B6)}$$

which has been demonstrated to agree well with the SBEs simulations. For a certain ionization channel $k' = k_l$, the integral is mainly contributed by the wavelets around the ionization time $t' = t_i$ which satisfy the phase slow-varying condition. To discuss the effect of GDD, we Taylor expand the phase S up to the fourth order at the ionization time:

$$S(k', t, t') = \sum_{n=0}^{4} \frac{\partial_{t'}^n S \mid_{t'=t_i}}{n!} (t' - t_i)^n + O[(t' - t_i)^5], \quad \text{(B7)}$$

with two terms involving the GDD $\frac{1}{6} F^3(t_i) \int_{t_i}^{t} \partial_k^3 \Delta\varepsilon_{cv}$ $(k', \tau, t_i) d\tau (t' - t_i)^3$ and $\frac{1}{4} F^2(t_i) \frac{\partial F}{\partial t'} \mid_{t'=t_i} \int_{t_i}^{t} \partial_k^3 \Delta\varepsilon_{cv}(k', \tau, t_i)$ $d\tau (t' - t_i)^4$. By discarding these two terms in the expansion, we can artificially eliminate the contribution of GDD to the phase of wavelets ionized in the vicinity of t_i. From these two terms, we can know that the GDD has a third- or higher-order effect on the electron movement, which is significantly weaker than that of GVD. Besides, the contribution of GDD is expo-

nentially dependent on the electric field strength. Therefore, we adopt a relatively strong field strength $F_0 = 0.008$ a.u. and $\omega_0 = 0.02$ a.u. to obtain a significant contribution.

Figure 13(d) shows the GDD of ZnO energy band, which is symmetric with respect to the zero. This implies that the accumulation of GDD during the acceleration process of electron-hole pairs will be offset to a great extent [seen in Fig. 12(f)]. Therefore, for the ZnO energy band, the effect of GDD for small ionization momentum is negligible. To discuss the effects of GDD qualitatively, we consciously choose an ionization channel which is far away from the zero, i.e., $k_l = 0.15 \frac{2\pi}{a_0}$ as marked with the black dashed line. In this way, the effect of GDD can be maintained.

As shown in Figs. 13(a)–13(c), we numerically integrate Eq. (B6) under the three scenarios: (a) using the accurate phase S (full phase); (b) using the phase of Taylor expansion (B7) including the GDD terms; (c) using the phase of Taylor expansion (B7) but discarding the GDD terms. Note that these results are plotted without normalization and with the same color bar for comparison. One can see that the emission distribution and intensity without the GDD is apparently different from the first two cases. For clarity, we show the emission distribution at $t_r = 0.28\ T_0$ in Fig. 13(e). One can see that the emission intensity without GDD (blue dotted line) is much larger than that of full phase (black line) and with GDD (red dotted line). Besides, the central emission energy for the case without GDD is slightly shifted as marked with blue vertical dashed line. These phenomena can be understood as follows.

From Eq. (B7), we know that the GDD can affect the phase of wavelets in the vicinity of t_i. In Fig. 13(f), we compare the full phase (black line) with the expanded phase including
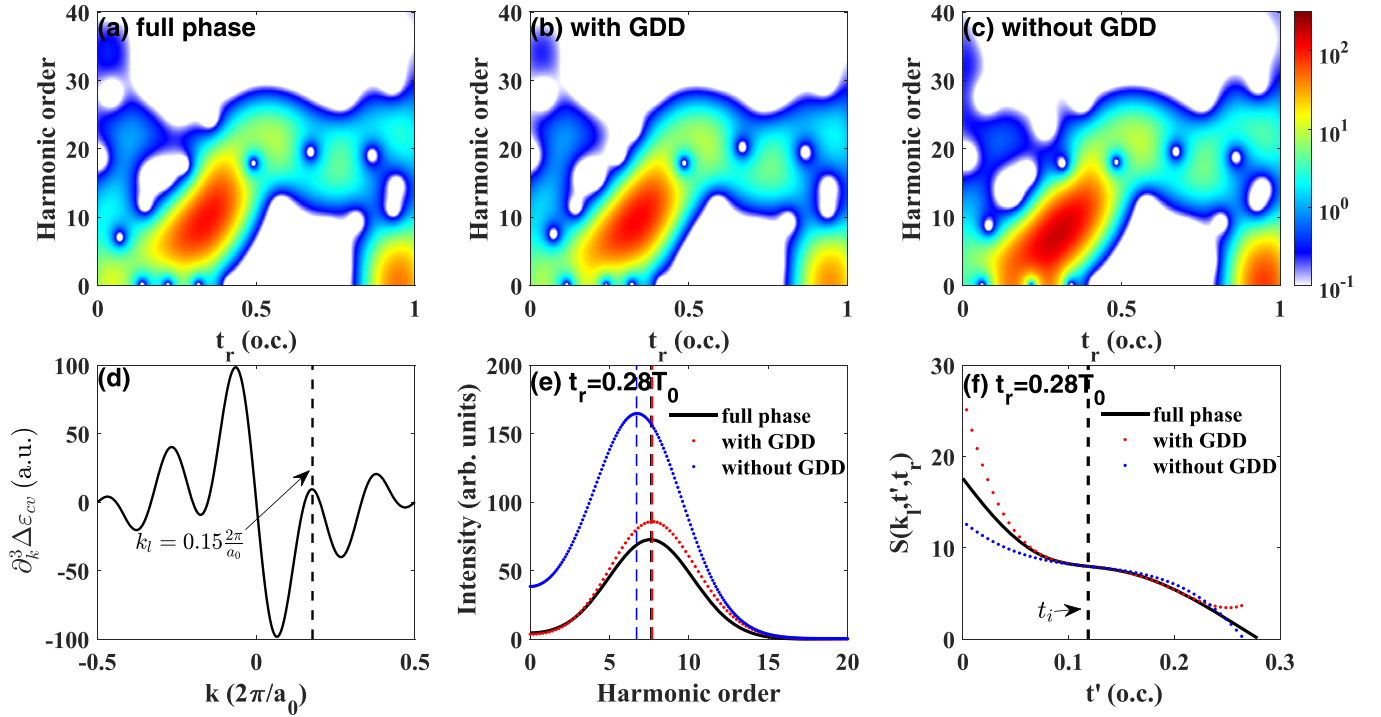
FIG. 13. (a)–(c) The time-frequency spectra obtained by numerically integrating Eq. (B6) under the three scenarios: (a) using the full phase; (b) using the phase of Taylor expansion including the GDD terms; (c) using the phase of Taylor expansion but discarding the GDD terms. (d) The GDD of ZnO energy band. (e) The emission distribution at $t_r = 0.28\,T_0$ for the cases in (a)–(c). (f) The phase of wavelets ionized at different time t' for $t_r = 0.28\,T_0$.

(red line) and not including (blue line) the GDD. One can see that the phase without GDD departs observably from the full phase, and shows a more slow-varying tendency, especially for $t' < t_i$. This implies that more wavelets will participate in the constructive interference, especially for the wavelets ionized ahead of t_i. As a result, the emission intensity is enhanced overall, and has a slower decay for the emission below the central emission energy. In addition, the central emission energy shows a slight shift to lower frequency; this can also be attributed to the joint contribution of the more slow-varying phase and larger ionization ($[F(t') = F_0\cos(\omega_0 t')]$) and emission amplitudes of wavelets which emit HHG below the central emission energy. These results indicate the important role of GDD in the detailed interference structure of HHG emission. We expect that the effect of GDD can be found to be non-negligible in some systems, e.g., the systems without the symmetric GDD, in the future.

APPENDIX C: SOLVING EQUATION BY FOURIER SERIES EXPANSION

Here, we solve Eqs. (5) and (6) using finite-order Fourier series expansion. The integrals in these equations contain nested trigonometric functions, which are challenging to solve exactly. Considering their periodicity with respect to ϕ, it can be analyzed qualitatively using the finite-order Fourier series expansion. For brevity, we denote the product of lattice constant a_0 and laser vector potential A_0 as b. The integral in the expression of classical displacement can be expanded as follows:

$$
\begin{aligned}
x_c =& \int_{\phi_i}^{\phi_r} -\sin[b(\sin\phi - \sin\phi_i)]d\phi \\
=& 2J_0(b)J_1(b)[\sin\phi_i(\phi_r - \phi_i) + \cos\phi_r - \cos\phi_i] \\
&+ 2J_1(b)J_2(b)[2(\cos2\phi_r - \cos2\phi_i)\cos2\phi_i \\
&+ \sin\phi_i(\sin2\phi_r - \sin2\phi_i)] \\
&+ 2J_0(b)J_3(b)[1/3(\cos3\phi_r - \cos3\phi_i) \\
&+ \sin3\phi_i(\phi_r - \phi_i)] \\
&+ \cdots .
\end{aligned}
\tag{C1}
$$

The expanded formula is still coupled for $\phi_i(b)$ and hard to solve exactly. Fortunately, we are primarily interested in the parameter dependence of $\phi_i(b)$, eliminating the need for an exact solution. Therefore, an approximate solution is enough. We can see that the dependence of x_c on the parameters b is mainly determined by the Bessel coefficient parts, while its dependence on phase ϕ_i is much weaker because the ionization usually occurs at the neighborhood of the peak of the field. Moreover, only the first term is dominant, and the other higher-order terms are much smaller. Consequently, we only retain the precise form of $\phi_i(b)$ for the first term and use an averaged ionization phase $\bar{\phi}_i(b)$ in other terms. This approach maintains the primary monotonicity in Eqs. (5) and (6) and simplifies the problem. We define $\eta(\phi_i^c) = \sin\phi_i(\phi_r - \phi_i^c) + \cos\phi_r - \cos\phi_i^c$, a monotonic function within our range of interest that can represent the relative value of ϕ_i. Consequently, we can approximately solve Eqs. (5) and (6). For the CSPM,

$x_c = 0$, we obtain

$$\eta\big[\phi_i^c(b)\big] \sim \frac{J_2(b)}{J_0(b)}\theta_{12}\big(\bar{\phi}_i^c\big) + \frac{J_3(b)}{J_1(b)}\theta_{03}\big(\bar{\phi}_i^c\big) + \cdots, \quad (C2)$$

where θ_{12} and θ_{03} represent the corresponding trigonometric function parts of Eq. (C1). For the WSPM, $x_c[\phi_i^w, \phi_r, b] = \bar{R}_{eh}[\phi_i^w, \phi_r, b]$, and the right-hand side can also be expanded as

$$\begin{aligned}
\bar{R}_{eh}\big(\phi_i^w, \phi_r, b\big) \sim{}& bJ_0^2(b)\big(\phi_r - \phi_i^w\big) \\
&+ 2bJ_0(b)J_2(b)\big[\tfrac{1}{2}\big(\sin 2\phi_r - \sin 2\phi_i^w\big) \\
&+ \big(\phi_r - \phi_i^w\big)\cos 2\phi_i^w\big] \\
&- 4bJ_1^2(b)\sin\phi_i^w\big(\cos\phi_r - \cos\phi_i^w\big) + \cdots.
\end{aligned}$$
$$(C3)$$

Similarly, we denote the trigonometric function parts in the above formulas as χ_{nm}, where n and m correspond to the orders of the Bessel coefficients. For a qualitative analysis, we only focus on the dominant terms, and obtain the solution

$$\begin{aligned}
\eta\big[\phi_i^w(b)\big] \sim{}& \frac{bJ_0(b)}{J_1(b)}\chi_{00}\big(\bar{\phi}_i^w\big) + \frac{bJ_2(b)}{J_1(b)}\chi_{02}\big(\bar{\phi}_i^w\big) \\
&+ \frac{bJ_1(b)}{J_0(b)}\chi_{11}\big(\bar{\phi}_i^w\big)\dots.
\end{aligned}$$
$$(C4)$$

When comparing Eqs. (C3) and (C4), it is evident that ϕ_i^c and ϕ_i^w exhibit different dependencies on the laser parameters, attributable to the presence of the electron-hole displacement $\bar{R}_{eh}$ introduced by the GVD.

[1] M. Ferray, A. L'Huillier, X. F. Li, L. A. Lompre, G. Mainfray, and C. Manus, Multiple-harmonic conversion of 1064 nm radiation in rare gases, J. Phys. B: At. Mol. Opt. Phys. **21**, L31 (1988).

[2] P. á. Corkum and F. Krausz, Attosecond science, Nat. Phys. **3**, 381 (2007).

[3] S. Ghimire, A. D. DiChiara, E. Sistrunk, P. Agostini, L. F. DiMauro, and D. A. Reis, Observation of high-order harmonic generation in a bulk crystal, Nat. Phys. **7**, 138 (2011).

[4] H. Liu, Y. Li, Y. S. You, S. Ghimire, T. F. Heinz, and D. A. Reis, High-harmonic generation from an atomically thin semiconductor, Nat. Phys. **13**, 262 (2017).

[5] N. Yoshikawa, T. Tamaya, and K. Tanaka, High-harmonic generation in graphene enhanced by elliptically polarized light excitation, Science **356**, 736 (2017).

[6] T. T. Luu, M. Garg, S. Y. Kruchinin, A. Moulet, M. T. Hassan, and E. Goulielmakis, Extreme ultraviolet high-harmonic spectroscopy of solids, Nature (London) **521**, 498 (2015).

[7] Y. S. You, Y. Yin, Y. Wu, A. Chew, X. Ren, F. Zhuang, S. Gholam-Mirzaei, M. Chini, Z. Chang, and S. Ghimire, High-harmonic generation in amorphous solids, Nat. Commun. **8**, 724 (2017).

[8] T. T. Luu, Z. Yin, A. Jain, T. Gaumnitz, Y. Pertot, J. Ma, and H. J. Wörner, Extreme–ultraviolet high–harmonic generation in liquids, Nat. Commun. **9**, 3723 (2018).

[9] J. Li, J. Lu, A. Chew, S. Han, J. Li, Y. Wu, H. Wang, S. Ghimire, and Z. Chang, Attosecond science based on high harmonic generation from gases and solids, Nat. Commun. **11**, 2748 (2020).

[10] G. Vampa, T. J. Hammond, N. Thiré, B. E. Schmidt, F. Légaré, C. R. McDonald, T. Brabec, D. D. Klug, and P. B. Corkum, All-optical reconstruction of crystal band structure, Phys. Rev. Lett. **115**, 193603 (2015).

[11] L. Li, P. Lan, L. He, W. Cao, Q. Zhang, and P. Lu, Determination of electron band structure using temporal interferometry, Phys. Rev. Lett. **124**, 157403 (2020).

[12] A. A. Lanin, E. A. Stepanov, A. B. Fedotov, and A. M. Zheltikov, Mapping the electron band structure by intraband high-harmonic generation in solids, Optica **4**, 516 (2017).

[13] T. T. Luu and H. J. Wörner, Measurement of the berry curvature of solids using high-harmonic spectroscopy, Nat. Commun. **9**, 916 (2018).

[14] H. B. Banks, Q. Wu, D. C. Valovcin, S. Mack, A. C. Gossard, L. Pfeiffer, R.-B. Liu, and M. S. Sherwin, Dynamical birefringence: Electron-hole recollisions as probes of berry curvature, Phys. Rev. X **7**, 041042 (2017).

[15] S. Jiang, J. Chen, H. Wei, C. Yu, R. Lu, and C. D. Lin, Role of the transition dipole amplitude and phase on the generation of odd and even high-order harmonics in crystals, Phys. Rev. Lett. **120**, 253201 (2018).

[16] Y.-T. Zhao, S. yan Ma, S.-C. Jiang, Y.-J. Yang, X. Zhao, and J.-G. Chen, All-optical reconstruction of k-dependent transition dipole moment by solid harmonic spectra from ultrashort laser pulses, Opt. Express **27**, 34392 (2019).

[17] K. Uchida, V. Pareek, K. Nagai, K. M. Dani, and K. Tanaka, Visualization of two-dimensional transition dipole moment texture in momentum space using high-harmonic generation spectroscopy, Phys. Rev. B **103**, L161406 (2021).

[18] M. Hohenleutner, F. Langer, O. Schubert, M. Knorr, U. Huttner, S. W. Koch, M. Kira, and R. Huber, Real-time observation of interfering crystal electrons in high-harmonic generation, Nature (London) **523**, 572 (2015).

[19] G. Vampa, T. Hammond, N. Thiré, B. Schmidt, F. Légaré, C. McDonald, T. Brabec, and P. Corkum, Linking high harmonics from gases and solids, Nature (London) **522**, 462 (2015).

[20] K. J. Schafer, B. Yang, L. F. DiMauro, and K. C. Kulander, Above threshold ionization beyond the high harmonic cutoff, Phys. Rev. Lett. **70**, 1599 (1993).

[21] G. Vampa, C. R. McDonald, G. Orlando, D. D. Klug, P. B. Corkum, and T. Brabec, Theoretical analysis of high-harmonic generation in solids, Phys. Rev. Lett. **113**, 073901 (2014).

[22] G. Vampa, C. R. McDonald, G. Orlando, P. B. Corkum, and T. Brabec, Semiclassical analysis of high harmonic generation in bulk crystals, Phys. Rev. B **91**, 064302 (2015).

[23] M. S. Mrudul, A. Pattanayak, M. Ivanov, and G. Dixit, Direct numerical observation of real-space recollision in high-order harmonic generation from solids, Phys. Rev. A **100**, 043420 (2019).

[24] E. N. Osika, A. Chacón, L. Ortmann, N. Suárez, J. A. Pérez-Hernández, B. Szafran, M. F. Ciappina, F. Sols, A. S. Landsman, and M. Lewenstein, Wannier-bloch approach to localization in high-harmonics generation in solids, Phys. Rev. X **7**, 021017 (2017).

[25] Y. S. You, D. A. Reis, and S. Ghimire, Anisotropic high-harmonic generation in bulk crystals, Nat. Phys. **13**, 345 (2017).

[26] R. Zuo, A. Trautmann, G. Wang, W.-R. Hannes, S. Yang, X. Song, T. Meier, M. Ciappina, H. T. Duc, and W. Yang,

Neighboring atom collisions in solid-state high harmonic generation, Ultrafast Science **2021**, 9861923 (2021).

[27] Y. S. You, E. Cunningham, D. A. Reis, and S. Ghimire, Probing periodic potential of crystals via strong-field re-scattering, J. Phys. B: At. Mol. Opt. Phys. **51**, 114002 (2018).

[28] L. Li, P. Lan, X. Zhu, T. Huang, Q. Zhang, M. Lein, and P. Lu, Reciprocal-space-trajectory perspective on high-harmonic generation in solids, Phys. Rev. Lett. **122**, 193901 (2019).

[29] L. Yue and M. B. Gaarde, Imperfect recollisions in high-harmonic generation in solids, Phys. Rev. Lett. **124**, 153204 (2020).

[30] L. Li, P. Lan, X. Zhu, and P. Lu, Huygens-fresnel picture for high harmonic generation in solids, Phys. Rev. Lett. **127**, 223201 (2021).

[31] X. Zhang, J. Li, Z. Zhou, S. Yue, H. Du, L. Fu, and H.-G. Luo, Ellipticity dependence transition induced by dynamical bloch oscillations, Phys. Rev. B **99**, 014304 (2019).

[32] Y. Feng, S. Shi, J. Li, Y. Ren, X. Zhang, J. Chen, and H. Du, Semiclassical analysis of ellipticity dependence of harmonic yield in graphene, Phys. Rev. A **104**, 043525 (2021).

[33] L. Li, P. Lan, X. Zhu, and P. Lu, High harmonic generation in solids: particle and wave perspectives, Rep. Prog. Phys. **86**, 116401 (2023).

[34] M. V. Berry, Quantal phase factors accompanying adiabatic changes, Proc. R. Soc. London A **392**, 45 (1984).

[35] D. Xiao, M.-C. Chang, and Q. Niu, Berry phase effects on electronic properties, Rev. Mod. Phys. **82**, 1959 (2010).

[36] C. Qian, C. Yu, S. Jiang, T. Zhang, J. Gao, S. Shi, H. Pi, H. Weng, and R. Lu, Role of shift vector in high-harmonic generation from noncentrosymmetric topological insulators under strong laser fields, Phys. Rev. X **12**, 021030 (2022).

[37] M. S. Mrudul and G. Dixit, High-harmonic generation from monolayer and bilayer graphene, Phys. Rev. B **103**, 094308 (2021).

[38] I. Al-Naib, J. E. Sipe, and M. M. Dignam, High harmonic generation in undoped graphene: Interplay of inter- and intraband dynamics, Phys. Rev. B **90**, 245423 (2014).

[39] L. Yue and M. B. Gaarde, Structure gauges and laser gauges for the semiconductor bloch equations in high-order harmonic generation in solids, Phys. Rev. A **101**, 053411 (2020).

[40] S. Jiang, H. Wei, J. Chen, C. Yu, R. Lu, and C. D. Lin, Effect of transition dipole phase on high-order-harmonic generation in solid materials, Phys. Rev. A **96**, 053850 (2017).

[41] D. Dimitrovski, L. B. Madsen, and T. G. Pedersen, High-order harmonic generation from gapped graphene: Perturbative response and transition to nonperturbative regime, Phys. Rev. B **95**, 035405 (2017).

[42] A. Chacón, D. Kim, W. Zhu, S. P. Kelly, A. Dauphin, E. Pisanty, A. S. Maxwell, A. Picón, M. F. Ciappina, D. E. Kim, C. Ticknor, A. Saxena, and M. Lewenstein, Circular dichroism in higher-order harmonic generation: Heralding topological phases and transitions in chern insulators, Phys. Rev. B **102**, 134115 (2020).